



## Full Length Article

Regulation of chemical microenvironment to overcome strength-ductility trade-off in FeCrVTiSi<sub>x</sub> high-entropy alloys coating

Shouyuan Lin <sup>a</sup>, Yuan Yao <sup>a,\*</sup>, Zhongping Yao <sup>a</sup>, Guanghui Shi <sup>a</sup>, Yanyan Liu <sup>a</sup>, Peng Zhang <sup>a</sup>, Songtao Lu <sup>a</sup>, Wei Qin <sup>b,\*</sup>, Xiaohong Wu <sup>a,\*</sup>

<sup>a</sup> MIIT Key Laboratory of Critical Materials Technology for New Energy Conversion and Storage, School of Chemistry and Chemical Engineering, Harbin Institute of Technology, Harbin 150001, PR China

<sup>b</sup> National Key Laboratory of Materials Behavior and Evaluation Technology in Space Environments, School of Materials Science and Engineering, Harbin Institute of Technology, Harbin 150001, PR China

## ARTICLE INFO

## Keywords:

Strength  
Ductility  
High-entropy alloys  
Density functional theory  
Valence electron concentration

## ABSTRACT

Developing metallic materials with both high strength and ductility is an enormous challenge in the field of materials science and engineering due to commonly known “strength-ductility trade-off”. In this work, we proposed a regulation strategy of the chemical microenvironment through changing valence electron concentration (VEC) to achieve simultaneous improvement of the strength and ductility of metallic materials. Taking FeCrVTiSi<sub>x</sub> system as a proof-of-concept model, we first predicted the influence of Si on the chemical microenvironment through density functional theory calculations. These calculations unveiled that Si atoms effectively modify the bonding state among alloy elements, resulting in an enhancement of the strength within the FeCrVTi alloy system while maintaining its ductility. Building upon this insight, we successfully synthesized FeCrVTiSi<sub>x</sub> alloys coating using laser cladding techniques. Subsequent tests, including nanoindentation, Vickers hardness, and tensile assessments, unequivocally demonstrated that the introduction of Si significantly increases the strength of the alloy while maintaining its ductility. Si atoms play a pivotal role in modulating the slip behavior of high-entropy alloys (HEAs) by reshaping the chemical microenvironment, thus enabling the elevation of strength in HEAs while preserving ductility. This work provides a novel approach for designing HEAs that effectively circumvent the “strength-ductility trade-off”, potentially broadening the horizons of engineering applications for HEAs coating.

## 1. Introduction

For metallic materials, the strength enhancement often leads to ductility loss, and vice versa [1–3]. This intrinsic drawback of metallic materials seriously limits their practical applications. Therefore, overcoming the “strength-ductility trade-off” in metallic materials is considered as one of the eternal pursuits in materials science and engineering [4]. Scientists have proposed various strategies to mitigate the “strength-ductility trade-off” dilemma to some extent [5], including second-phase precipitation [2,6,7], gradient structures [8–10], alloying [11–13], grain refinement [14–16], twinning [17–19], and heat treatment [20–22]. However, fully resolving the “strength-ductility trade-off” remains a formidable challenge.

It is well-known that hindering the movement of dislocations can enhance the strength of metallic materials, whereas ductility

necessitates effective dislocation sliding, thus giving rise to the “strength-ductility trade-off” at the microscopic level [17,23]. Within metallic materials, the relative motion of dislocations between different atoms can be understood as a continuous process including the breaking of old bonds and the formation of new ones. This process is closely related to the surrounding chemical microenvironment of the atoms. When the chemical microenvironment promotes the breaking of old bonds and the formation of new ones, dislocations can slide effectively, resulting in favorable ductility. Conversely, if the chemical microenvironment impedes the breaking of old bonds or the formation of new ones, dislocation movement can be seriously hindered to enhance the strength. Therefore, it is reasonable to tune the surrounding chemical microenvironment of metal atoms in metallic materials to achieve the mitigation of the “strength-ductility trade-off”. The keys to this strategy are what kind of alloys possess tunable chemical microenvironment and

\* Corresponding authors.

E-mail addresses: [yyuan@hit.edu.cn](mailto:yyuan@hit.edu.cn) (Y. Yao), [qinwei@hit.edu.cn](mailto:qinwei@hit.edu.cn) (W. Qin), [wuxiaohong@hit.edu.cn](mailto:wuxiaohong@hit.edu.cn) (X. Wu).

what kind of elements can regulate the chemical microenvironment of alloys.

High-entropy alloys (HEAs), as a category of multi-component solid solution alloys [24,25], exhibit promising potential for diverse applications due to their radiation resistance [26], corrosion resistance [27], and other properties [28,29]. Inevitably, HEAs are also confronted with the “strength-ductility trade-off”. For instance, NbMoTaW demonstrates high strength but limited ductility [30], while CoCrFeNiMn exhibits excellent ductility but comparatively low strength [28]. HEAs are composed of multiple metallic elements, and the chemical microenvironment surrounding the atoms is directly influenced by neighboring atoms, offering an avenue for tuning this environment. Si, as a non-metallic element, possesses notably distinct physicochemical properties compared to metallic elements. The outer valence electrons of Si element reside in a semi-filled state, and have much lower valence electron concentration (VEC) than most of metallic elements. These characteristics render Si capable of effectively influencing the strength of chemical bonds in metallic materials and adjusting the chemical microenvironment of HEAs system to regulate dislocation sliding, exhibiting promising potential to enhance both strength and ductility of HEAs. For example, Lin et al. identified that the introduction of Si in the FeCoCrNi alloy system formed solid solution strengthening to significantly enhance the mechanical properties by dislocation loop strengthening mechanisms [31]. Wei et al. observed that the introduction of Si not only governs the plastic deformation of the CoCrFeNi HEA system but also elevates the yield stress through various strengthening mechanisms [32]. Wei et al. developed a new type of  $\text{Fe}_{26.7}\text{Co}_{26.7}\text{Ni}_{26.6}\text{B}_{11}\text{Si}_0$  high-entropy metallic glass with impressive bend ductility [12]. Additionally, Hou et al. found that the addition of Si markedly improves the strength and ductility of the  $\text{Fe}_{50}\text{Mn}_{30}\text{Co}_{10}\text{Cr}_{10}$  metastable HEA. It is mainly attributed to the synergistic effects of multiple mechanisms, including dislocation and stacking fault interactions [11]. These research findings serve as a foundation for adjusting the chemical microenvironment of the alloy system to effectively control dislocations, thereby enhancing the strength and ductility of metallic materials.

In this study, we present a strategy grounded in valence electron concentration to tune the chemical microenvironment, achieving the mitigation of the “strength-ductility trade-off” in HEAs coating. Taking FeCrVTiSi<sub>x</sub> HEAs as the proof-of-concept model, the influence of Si on the chemical microenvironment of HEAs was first validated through density functional theory calculations, utilizing techniques such as quasi-harmonic approximation Debye model, electron localization function (ELF), and density of states (DOS). Then, the relation of the chemical microenvironment with the mechanical properties and ductility was predicted. Finally, the experimental studies including the synthesis and property characterizations of FeCrVTiSi<sub>x</sub> alloy coating were conducted to support the theoretical prediction. The obtained results may pave the way to mitigate the “strength-ductility trade-off” in metallic coatings and expand their practical applications in many fields.

## 2. Computational methodology and experiment details

### 2.1. Computational methodology

To establish a rational structure for HEAs and model the random distribution of their constituent elements, we refined the Warren-Cowley short-range order (SRO) parameters which were achieved through the use of the Alloy Theoretic Automated Toolkit (ATAT) [33] utilizing a Monte Carlo simulated annealing algorithm [34]. Our focus was directed towards FeCrVTiSi<sub>x</sub> HEAs, characterized by a body-centered cubic (BCC) crystal structure. Here, ‘x’ denotes the molar ratio, with values of 0, 0.5, 1.0, 1.5 and 2.0 abbreviated respectively as Si<sub>0</sub>, Si<sub>0.5</sub>, Si<sub>1.0</sub>, Si<sub>1.5</sub>, and Si<sub>2.0</sub> for ease of reference. Table S1 illustrates the relationship between the Si content and the configuration entropy in the FeCrVTiSi<sub>x</sub> system. Aiming to strike an optimal balance between computational resources and the pragmatic needs of the simulated HEAs

structures, we constructed a  $4 \times 4 \times 4$  supercell unit, encompassing a total of 128 atoms.

The density functional theory calculations were performed through the Perdew-Burke-Ernzerhof (PBE) [35] functional for exchange-correlation potentials and ion-electron interactions within the generalized gradient approximation (GGA) and using the Vienna Ab-initio Simulation Package (VASP) [36,37]. In this work, the plane-wave cut-off energy was set to 500 eV, the Brillouin zone K-point grid to  $2 \times 2 \times 2$  using the Gamma-centered scheme for static self-consistent calculations, and the volume and atomic positions of the supercell were optimized until the residual stress on each atom was less than 0.01 eV/Å.

We derived a series of elastic constants using the stress-strain method to ascertain the mechanical properties of the FeCrVTiSi<sub>x</sub> HEAs system [38]. The prediction of mechanical performance, grounded in Hooke's law [39], has been effectively utilized for calculating the mechanical properties of diverse alloys. Within the BCC crystal structure, three independent elastic constants ( $C_{11}$ ,  $C_{12}$ , and  $C_{44}$ ) are required for the prediction of key mechanical properties: bulk modulus ( $B$ ), shear modulus ( $G$ ), Young's modulus ( $E$ ), Poisson ratio ( $\nu$ ), Vickers hardness ( $H_v$ ) and fracture toughness ( $K_{IC}$ ) [40–44]. The bulk modulus  $B$  can be expressed as:

$$B = \frac{C_{11} + 2C_{12}}{3} \quad (1)$$

The shear modulus  $G$  can be expressed as:

$$G = \frac{GV + GR}{2}, GV = \frac{C_{11} - C_{12} + 3C_{44}}{5}, GR = \frac{5(C_{11} - C_{12})C_{44}}{4C_{44} + 3(C_{11} - C_{12})} \quad (2)$$

The Young's modulus  $E$  and Poisson ratio  $\nu$  can be expressed as:

$$E = \frac{9BG}{3B + G}, \nu = \frac{3B - 2G}{2(3B + G)} \quad (3)$$

Without considering the energy dissipation during mechanical loading, the expressions for Vickers hardness  $H_v$  and the calculated fracture toughness  $K_{IC}$  are given respectively as:

$$HV = 0.92 \left( \frac{G}{B} \right)^{1.137} G^{0.708}, K_{IC} = V_0^{1/6} G \left( \frac{B}{G} \right)^{1/2} \quad (4)$$

where  $V_0$  represents the volume per atom.

For examining the thermal stability of FeCrVTiSi<sub>x</sub>, we subjected the Si<sub>2.0</sub> structural model, containing 128 atoms, to ab-initio molecular dynamics (AIMD) simulations at two distinct temperatures: 550 °C and 1100 °C. The AIMD calculations were performed using DFT-based VASP after structural optimization, with simulations confined to the  $\Gamma$  point and a cutoff energy set at 500 eV. In these simulations, a canonical NVT ensemble with a Nose-Hoover thermostat was deployed for constant-temperature simulations at 823.15 K and 1373.15 K, respectively. The AIMD simulations were stopped after 10 ps, with a time step of 1 fs [45].

Our study utilized the quasi-harmonic Debye model to explore the impact of temperature variations on the Debye temperature and other thermodynamic properties of HEAs. These calculations were primarily achieved through density functional theory calculations combined with the GIBBS2 code [46]. Details about the GIBBS2 code can be found in Eq. S1.

### 2.2. Experimental preparation details

This study employed a 1Cr13 ferritic/martensitic steel substrate, sourced from Jiangsu Zhaolong Metal Products Co., Ltd., China. The dimensions of the substrate were 38 mm × 46 mm × 18 mm. The chemical composition of the substrate is detailed in Table S2. For coating preparation, the substrate surface was polished using 60-grit silicon carbide sandpaper to remove surface oxidation. The substrate was then ultrasonically cleaned in ethanol and dried, readying it for

further procedures.

The coating material comprised high-purity (>99.5 %) powders of Fe, Cr, V, Ti, and Si (35  $\mu\text{m}$  particle size), obtained from Shanghai Pantian Powder Materials Co., Ltd., China. Table S3 presents the basic properties of the component elements. These powders were mixed in a specific molar ratio to create the  $\text{FeCrVTiSi}_x$  compound. A planetary ball mill was employed to achieve a homogeneous mixture of the powders. Milling parameters included a speed of 400 rpm, intermittent milling (30 min on, 15 min off), totaling 50 h, and a ball-to-powder weight ratio of 10:1. Laser cladding was performed on the substrate surface using a pre-fabricated powder feeding method and a fiber laser (REL-C4000X, China). Table S4 outlines the specific parameters of the laser cladding process.

### 2.3. Characterization of high-entropy alloy coatings

Phase structures of HEA coatings were characterized via X-ray diffraction (XRD, Bruker D8, USA), employing  $\text{Cu K}\alpha$  radiation at 40 kV and 40 mA. Scans encompassed a 20 range from 20° to 90°, progressing at a rate of 7°/min with an incremental step size of 0.02°. Surface morphologies were scrutinized using a scanning electron microscope (SEM, Zeiss Supra 55, Germany), integrated with an energy-dispersive spectrometer (EDS) at an acceleration voltage of 15 kV. Microstructural characterizations were conducted via electron backscatter diffraction (EBSD) imaging and transmission electron microscopy (TEM). EBSD analyses utilized a field emission scanning electron microscope (Quanta 200FEG) with an EBSD detector, determining grain size distributions through the line intercept method. Samples for EBSD analysis were first ground to 4000 grit using different grades of SiC sandpaper, then mechanically polished with a colloidal silica suspension (0.02  $\mu\text{m}$ ), and finally electropolished with a mixed solution of  $\text{HClO}_4$ :  $\text{C}_2\text{H}_5\text{OH} = 1:9$  (volume ratio) at 293 K, with a polishing voltage of 25 V and a polishing time of 20 s. EBSD scanning was executed with a step size of 1.2  $\mu\text{m}$ . Crystallographic analysis employed a FEI Tecnai G2 F30 TEM, operated at a working voltage of 300 kV. TEM specimen preparation entailed mechanically thinning foils to 50  $\mu\text{m}$ , punching them into 3 mm discs, and further refining via ion-beam milling (Gatan 695) for electron transparency.

The microhardness evaluation was conducted using a Vickers hardness tester (HXD-1000TM/LCD, Shanghai Taiming Co., Ltd., China). After referencing the GB/T 4340.1-2009 and ISO 6507-1 standards and considering various factors such as ensuring the indentation depth is less than 10 % of the tested coating thickness, the practicalities of the instrument used, and the results of preliminary experiments, the test parameters were meticulously chosen to ensure the accuracy of the microhardness results. The final testing parameters were: a load of 9.8 N with a dwell time of 15 s. Each coating was measured five times at five different points, and the average of these values represents the final hardness. To determine the Young's modulus and microhardness of the coating, nanoindentation assessments, conducted at 25 °C using a Berkovich diamond indenter and based on the Oliver-Pharr method [47], yielded load-displacement curves and elastic moduli of the coatings. Parameters were set as loading rate of 0.1  $\text{s}^{-1}$ , hold time of 10 s, and indentation depth of 1000 nm. For the  $\text{Si}_0$ ,  $\text{Si}_{0.5}$ ,  $\text{Si}_{1.0}$ ,  $\text{Si}_{1.5}$ , and  $\text{Si}_{2.0}$  coatings, the loads applied to achieve an indentation depth of 1000 nm were 80, 98, 104, 115, and 175 mN, respectively. Replicate measurements at five discrete points on each coating were averaged to ascertain the final nanoindentation data. Notably, the maximum indentation depth remained below one-tenth of the coating thickness, minimizing substrate influence. Drift monitoring and correction were implemented pre-testing for enhanced data precision.

To assess the strength and elongation rate of the samples, tensile properties at room temperature were assessed employing an electronic universal testing machine (Instron 5569, USA), operating at a loading rate of 1 mm/min. Tensile test specimens, prepared from 1 mm thick coatings, conformed to ISO6892-1 dimensions with a gauge length of 15

mm and a cross-sectional area of  $1.9 \times 1 \text{ mm}^2$  [48,49]. Owing to the presence of a minor proportion of the substrate within the coating, the deformation behavior of the coating and the substrate during the tensile process is not consistent. Either the coating or the substrate tends to fracture first during stretching, as shown in Fig. S1, thereby precluding the use of extensometers. To ensure the accuracy of the test data, we calibrated the instrument prior to the initiation of the tensile tests to determine its compliance. This was achieved by preloading the instrument and recording its response to quantify the impact of the instrument's compliance on the measurement results. During data processing, the measured data were corrected based on the calibration results to eliminate the influence of the instrument's intrinsic compliance. This procedure guaranteed the precision of the experimental strain measurements. Each sample set was subjected to a minimum of three tensile tests to ascertain the reliability and repeatability of the results, with the mean value represented in the tensile curve. Post-tensile testing, fracture morphologies were characterized via SEM.

## 3. Results and discussion

### 3.1. Theoretical predictions derived from density functional theory calculations

#### 3.1.1. Structural model and stability

A rational structural model is critical to ensure the precision of DFT predictions in assessing the mechanical properties of materials. To model the stochastic nature of constituent elements in HEAs and further assess the influence of varying Si content on mechanical properties, we utilized the Special Quasirandom Structures (SQS) [50] method to enable the construction and optimization of BCC structural models of  $\text{FeCrVTiSi}_x$  alloys with varying Si concentrations, as illustrated in Figs. S2 and S3. The optimization results showed a random distribution of constituent elements within the solid solution structures. Fig. 1(a) shows the DFT-calculated lattice constants of 2.934, 2.930, 2.933, 2.939, and 2.948 Å for Si compositions ranging from  $\text{Si}_0$  to  $\text{Si}_{2.0}$ , respectively. These findings indicate that the addition of Si does not significantly change the lattice constant of the HEA. This was also supported by the calculated lattice constants using Vegard's law [38] as shown in Fig. 1(a), further validating the effectiveness of the SQS model. As one of the four core effects in HEAs, lattice distortion is defined as the deviation between actual atomic positions and their ideal lattice counterparts, as detailed in Eq. S2. Fig. 1(b) demonstrates that Si addition escalated the lattice distortion of HEAs from 0.025 Å/atom in  $\text{Si}_0$  to 0.044 Å/atom in  $\text{Si}_{2.0}$ , nearly a twofold increase. This augmentation is likely attributable to the fact that the Si atom, having a smaller atomic radius, can amplify atomic size mismatches and prompt greater deviations from ideal positions, thereby increasing lattice distortion. The increase in lattice distortion is beneficial for enhancing the mechanical properties of the alloy system and improving the ductility of BCC HEAs [51].

Stability is paramount for the practical implementation of structural materials in engineering contexts. To ascertain the chemical and thermodynamic stability of  $\text{FeCrVTiSi}_x$  HEAs, we calculated their formation enthalpy and cohesive energy, detailed in Eq. S3. Fig. 1(c) shows that the formation enthalpies of each system are negative, suggesting that the formation of the HEA solid solution from elemental metals is thermodynamically favorable. Table S5 presents a comparison of the enthalpy of formation and cohesive energy obtained in this study with those reported in the existing literature. Moreover, HEAs with different Si contents exhibit negative cohesive energies, suggesting that the system in the solid solution has lower energy than that in the isolated atoms, indicating the stability of the solid solution structure. To further assess the stability of  $\text{FeCrVTiSi}_x$  at high temperatures, we performed AIMD simulations on  $\text{Si}_{2.0}$ , which has a relatively high formation enthalpy. Figs. S4 and S5 compare the structural models before and after the AIMD simulation at 550 °C and 1100 °C. It was observed that at both

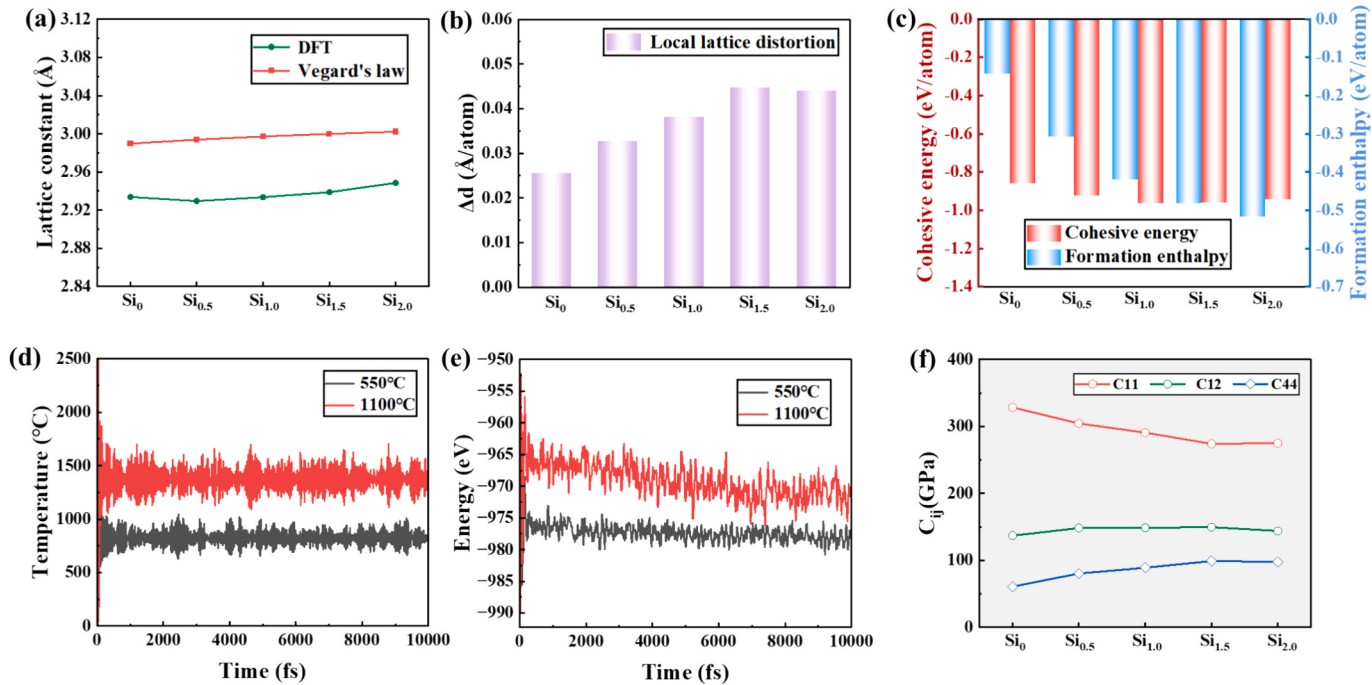


**Fig. 1.** Structural modeling and stability analysis of FeCrVTiSi<sub>x</sub>: (a) Comparison of calculated lattice constants with Vegard's law; (b) Local lattice distortion; (c) Formation enthalpies and cohesive energies of the HEAs; (d) Temperature variation over time for the Si<sub>2.0</sub> system during AIMD simulations; (e) Total energy variation over time for the Si<sub>2.0</sub> system during AIMD simulations; (f) Elastic constants: C<sub>11</sub>, C<sub>12</sub> and C<sub>44</sub>.

temperatures, the supercell crystal structure exhibits substantial distortion and partial disorder, yet the overarching lattice framework remains largely intact. The total energy and temperature of the system at different temperatures over time, as shown in Fig. 1(d) and (e), reveal that aside from initial fluctuations, the total energy and temperature of the system generally fluctuate steadily over time, indicating good thermal stability of the solid solution structure at high temperatures. Utilizing the stress-strain method on the optimized stable structure, we derived the elastic constant matrix, with results tabulated in Tables S6 to S10. For the BCC structure, the Born stability criteria [52] can be expressed as: C<sub>11</sub> > 0, C<sub>44</sub> > 0, C<sub>11</sub> - |C<sub>12</sub>| > 0, C<sub>11</sub> + 2C<sub>12</sub> > 0. The elastic constants of FeCrVTiSi<sub>x</sub> meet these criteria, affirming mechanical stability in the system.

The prognostication of mechanical properties is intrinsically linked to the elastic constants of HEAs. In BCC solid solution structures, three independent elastic constants are pivotal: C<sub>11</sub>, C<sub>12</sub>, and C<sub>44</sub>. Fig. 1(f) indicates that as Si content increases, C<sub>11</sub> initially decreases and then increases but C<sub>12</sub> and C<sub>44</sub> first rise and then fall. All of them reach regional extrema at Si<sub>1.5</sub>, with the minimum value of C<sub>11</sub> being 274.1 GPa, and the maximum values of C<sub>12</sub> and C<sub>44</sub> being 149.6 GPa and 99.1 GPa, respectively. This suggests that Si<sub>1.5</sub> may be a turning point for mechanical properties.

### 3.1.2. Chemical microenvironment

Chemical microenvironment is widely recognized as a key factor in the mechanical properties of materials. The influence of silicon with relatively low VEC on the chemical microenvironment of the FeCrVTiSi<sub>x</sub> HEAs was analyzed using the Debye temperature, ELF, and DOS, and the effects on mechanical properties were further determined. Firstly, the variation in the Debye temperature of the FeCrVTiSi<sub>x</sub> HEA as a function of temperature was calculated. The Debye temperature [53–55], a crucial physical parameter in solids, reflects the atomic binding force, correlating directly with properties like elasticity and hardness. As depicted in Fig. 2(a), the Debye temperature exhibits a gradual increase with increased silicon content. This suggests the increase of the covalent bond proportion in the system, thus enhancing the material's strength

properties.

ELF provides a quantitative description of the chemical microenvironment within a system [56]. For instance, the ELF value of 0.5 indicates typical metallic bond characteristics, while the value of 1 signifies complete covalent bond characteristics. ELF calculations were conducted to elucidate the impact of Si content on the chemical microenvironment. Figs. 2(b) and S6–7 reveal elevated ELF values around Si atoms, indicating a relatively high valence electron concentration and the heightened covalent bond proportion in the system. This is primarily due to the fact that Si element has much higher electronegativity than other metal atoms, fostering electron localization to form stronger covalent bonds, coupled with its semi-filled outermost valence electrons. In comparison, lower ELF values around Fe, Cr, V, and Ti atoms indicate more dispersed valence electrons, a hallmark of metallic bonds. Generally, metal atoms in the system tend to delocalize the valence electrons to form metallic bonds, whereas valence electrons in Si atoms tend to be localized, resulting in the formation of the covalent bonds. When the system is subjected to stress to induce dislocation slip, the delocalized valence electrons of metal atoms facilitate the movement of dislocations, maintaining the ductility of the system, while intensified covalent bonds near Si atoms increase dislocation movement resistance to enhance the strength, contributing to the mitigation of the “strength-ductility trade-off”. However, with a Si content of 2.0, increasing aggregation of Si atoms may trigger the intrinsic brittleness of Si element to potentially serve as a fracture initiation site, diminishing mechanical efficacy. Additionally, we examined the alterations in the DOS resulting from the introduction of Si, as depicted in Figs. 2(c–e) and S8–10. Fig. S7 illustrates the total DOS with a red dash line denoting the Fermi level. FeCrVTiSi<sub>x</sub> has a non-zero density at the Fermi level, exhibiting typical metal characteristic. Moreover, the position and shape of total DOS remain almost unchanged with the increasing Si content, signifying structural stability in the HEAs [57]. The PDOS reveals substantial hybridization between silicon and metal atoms, particularly between p orbitals of Si and d orbitals of metal elements, leading to the formation of hybridized bonds. Semi-filled outer valence electrons and pronounced electronegativity of Si element enable it to form robust

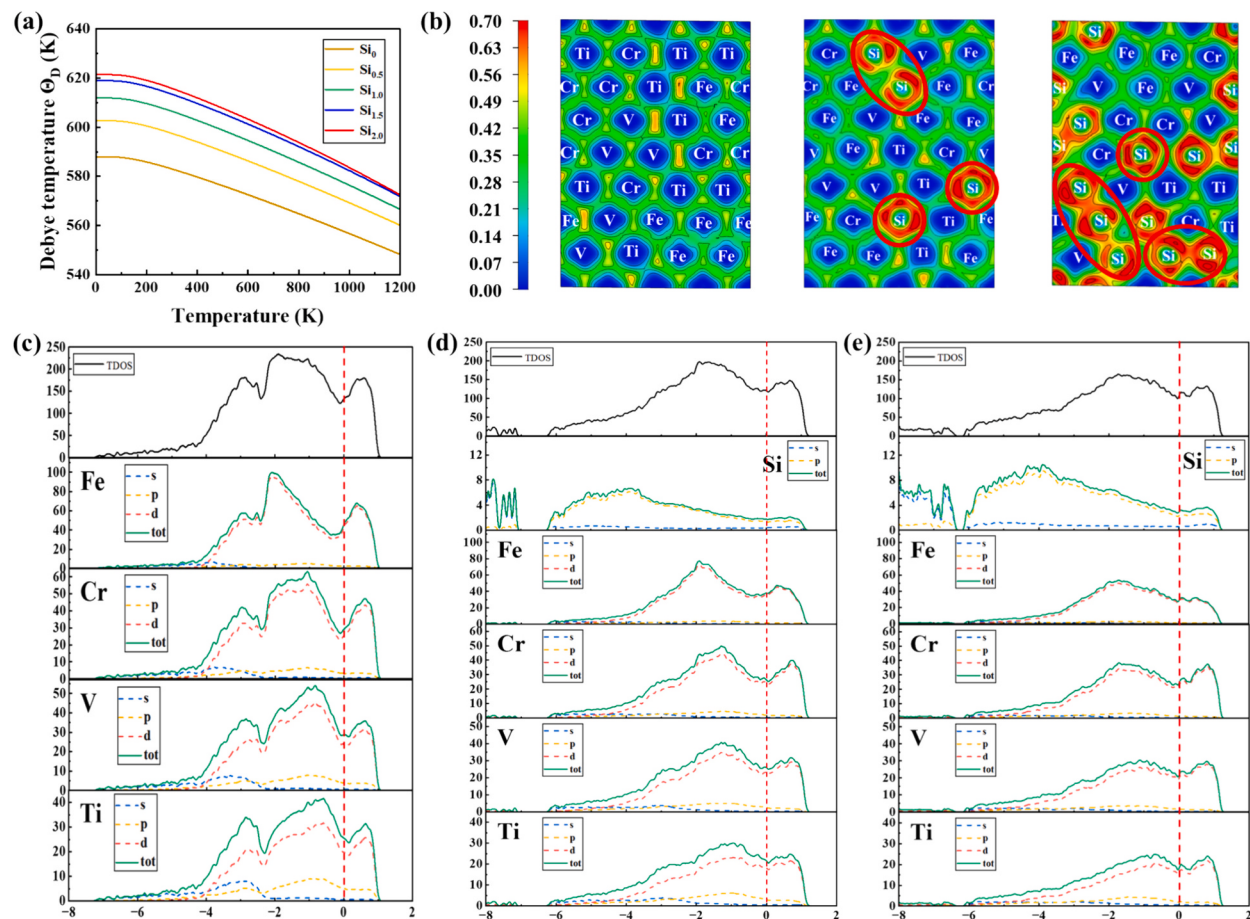


**Fig. 2.** Electronic structure analysis: (a) Temperature-dependent Debye temperature of  $\text{FeCrVTiSi}_x$ ; (b) ELF distribution maps for (110) plane, sequentially corresponding to  $\text{Si}_0$ ,  $\text{Si}_{1.0}$ , and  $\text{Si}_{2.0}$ , from left to right; (c) Partial density of states (PDOS) of  $\text{Si}_0$ ; (d) PDOS of  $\text{Si}_{1.0}$ ; and (e) PDOS of  $\text{Si}_{2.0}$ . The position of the Fermi energy level in (c-e) has been set to 0 eV and marked with a vertical dashed red line. (For interpretation of the references to colour in this figure legend, the reader is referred to the web version of this article.)

covalent bonds with other metal atoms. Concurrently, the inter-hybridization of metal atoms in d orbitals results in weaker valence bonds, preserving system ductility.

Based on the discussion above, one can see that silicon significantly regulates the chemical microenvironment of HEAs and further influences its mechanical properties. Specifically, silicon can form much stronger valence bonds with other metals via p-d orbital hybridization to increase the system's covalent bond proportion, stabilizing and enhancing the system's strength properties. Meanwhile, the metallic

bonds formed between metal atoms guarantee the system's ductility [58].

### 3.1.3. Calculated mechanical properties of $\text{FeCrVTiSi}_x$

Building upon the prior analysis that Si incorporation regulates the system's chemical microenvironment, mechanical properties were subsequently predicted. Fig. 3(a) delineates the variations in Young's modulus ( $E$ ), shear modulus ( $G$ ), Vickers hardness ( $H_v$ ), bulk modulus ( $B$ ), and fracture toughness ( $K_{IC}$ ) with the average VEC of the system.

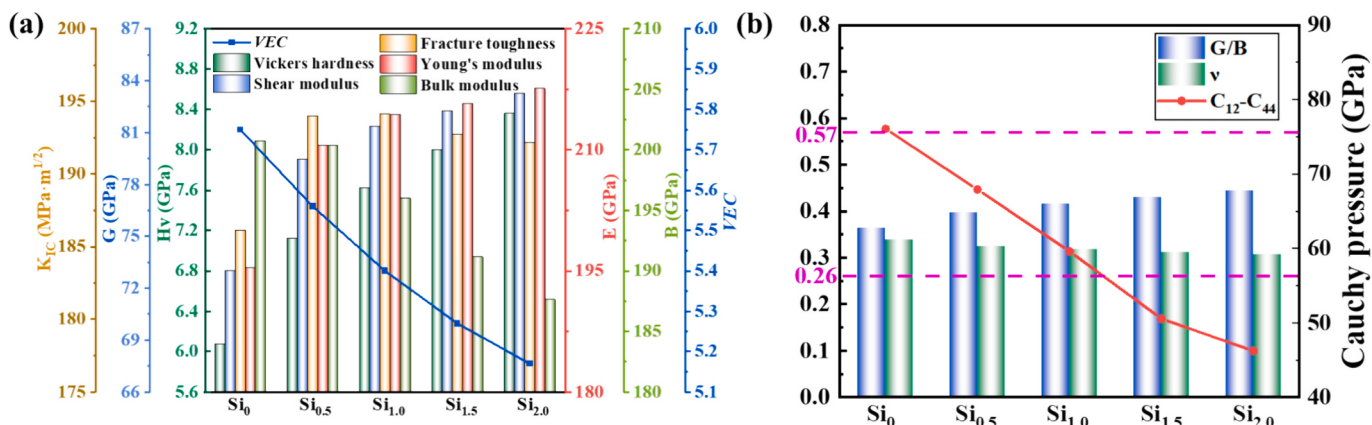


**Fig. 3.** (a) The variation of calculated mechanical properties with VEC in the system; (b) Ductility indicators:  $G/B$ , Poisson ratio  $v$ , and  $C_{12}-C_{44}$ .

The average VEC is defined as [59,60]:  $VEC = \sum_{i=1}^n c_i(VEC_i)$ , where  $c_i$  represents the component's proportion, and  $VEC_i$  denotes the count of valence electrons for component  $i$ . The computed  $VEC$  values for  $Si_0$ ,  $Si_{0.5}$ ,  $Si_{1.0}$ ,  $Si_{1.5}$ , and  $Si_{2.0}$  are 5.75, 5.56, 5.40, 5.27, and 5.17, respectively. Observations reveal that, except bulk modulus, the system's mechanical properties generally improve as the average valence electron concentration decreases, aligning with the previous suggestion that lower valence electron concentrations enhance the strength of HEAs [61]. Young's modulus escalated from 195 GPa in  $Si_0$  to 218 GPa in  $Si_{2.0}$ , marking an approximate 12 % increase; the shear modulus also enhanced with Si addition; Vickers hardness rose from 6.07 GPa in  $Si_0$  to 8.36 GPa in  $Si_{2.0}$ , a 37 % increment; and fracture toughness significantly improved compared to the Si-free scenario. Consequently, the introduction of Si, characterized by a lower  $VEC$ , effectively bolsters the strength of the alloy system.

The alloy system's ductility was also predicted through three indicators: the G/B ratio [62], Poisson ratio ( $\nu$ ) [63], and the difference between  $C_{12}$  and  $C_{44}$  ( $C_{12}-C_{44}$ ) [57], with results displayed in Fig. 3(b). The G/B ratios for the FeCrVTiSi<sub>x</sub> system range from 0.36 to 0.44, lower than the threshold of 0.57, indicative of ductile characteristics. Similarly, Poisson ratio values, ranging from 0.34 to 0.31, which exceed the threshold of 0.26, suggesting good ductility [63]. The  $C_{12}-C_{44}$  values are 76.1, 67.9, 59.6, 50.5, and 46.2 GPa, greater than 0, further confirming the system's ductility [57]. Therefore, the integration of Si into the FeCrVTi alloy system is anticipated to augment the alloy's strength while preserving its considerable ductility.

### 3.2. Phase composition and microstructure analysis

Guided by theoretical predictions using density functional theory calculations, we synthesized a range of HEA coatings using laser cladding. The XRD results of the coatings in Fig. 4(a) demonstrate the FeCrVTiSi<sub>x</sub> system as a single BCC solid solution phase, aligning with the Powder Diffraction File (PDF) standard (JCPDS#34-0396). The formation of the single-phase BCC solid solution can be attributed to the non-equilibrium solidification effect, a consequence of rapid heating and cooling during laser cladding. Additionally, by comparing various diffraction peaks, it can be observed that in solid solutions with varying silicon content, a preferential orientation along the (110) crystal planes is consistently present. Using the Bragg's equation, the lattice constants

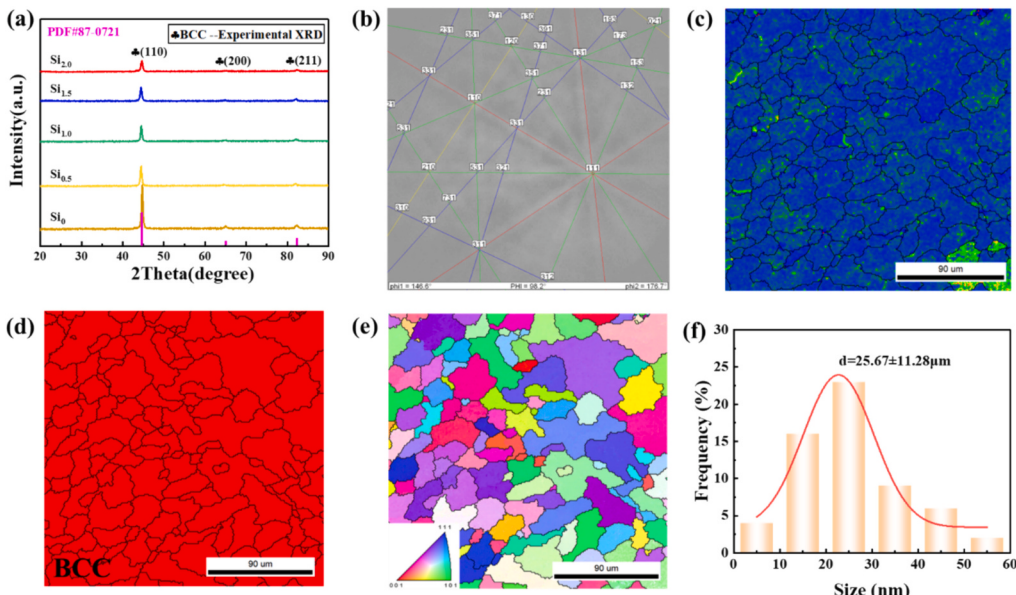
for  $Si_0$ ,  $Si_{0.5}$ ,  $Si_{1.0}$ ,  $Si_{1.5}$ , and  $Si_{2.0}$  were calculated to be 2.862, 2.878, 2.875, 2.878, and 2.868 Å, respectively. When compared to the results obtained from density functional theory calculations, the errors are 2.45 %, 1.77 %, 1.98 %, 2.08 %, and 2.71 %, demonstrating relatively small discrepancies.

Fig. 4(b-f) presents the EBSD characterization of  $Si_{1.5}$ . Fig. 4(b) displays the calibrated diffraction Kikuchi bands, while Fig. 4(c) and (d) show Kernel Average Misorientation (KAM) and phase distribution maps, respectively.  $Si_{1.5}$  is observed to exhibit a singular BCC phase, consistent with the XRD characterization. Fig. 4(f) illustrates the grain size distribution with average grain size for  $Si_{1.5}$  of  $25.67 \pm 11.28 \mu m$ .

Further, TEM was employed for enhanced structural characterization of  $Si_{1.5}$ , as illustrated in Fig. 5. Fig. 5(a) presents the bright-field TEM image of the coating, indicating a substantial dislocation density in  $Si_{1.5}$ . This observation is potentially attributable to lattice distortions arising from the inter-dissolution of different-size atoms and the release of residual stresses accrued during the laser cladding process [64,65]. Fig. 5 (b) depicts the SAED pattern along the [001] zone axis. The interplanar distances measured at three distinct points in the SAED pattern are 2.054 Å, 1.462 Å, and 2.033 Å, respectively. Comparison with the Powder Diffraction File standard card (JCPDS#34-0396) reveals these distances corresponding to the (110), (200), and  $(\bar{1}\bar{1}0)$  planes, respectively, substantiating that  $Si_{1.5}$  is a BCC phase solid solution. Fig. 5 (c) features a HRTEM image and its magnified version, demonstrating that the lattice configurations in all regions are consistent, proving that these regions are single-phase structures. This area corresponds to the (110) plane with an interplanar spacing of 2.013 Å, aligning with the previous SAED and standard PDF card, further endorsing the identification of  $Si_{1.5}$  as a BCC phase solid solution. Elemental surface analysis was conducted via EDS, as depicted in Fig. 5(d), revealing a homogeneous distribution of elements without noticeable segregation, corroborating the traits of a single-phase solid solution.

### 3.3. Experimental mechanical properties of FeCrVTiSi<sub>x</sub>

To investigate the influence of Si on the mechanical properties of HEAs, nanoindentation tests were conducted on the coatings. Load-displacement curves, depicted in Fig. 6(a), demonstrate that to attain a 1000 nm penetration depth, the required loads for  $Si_0$  to  $Si_{2.0}$  were 80, 98, 104, 115, and 175 mN, respectively. The load for  $Si_{2.0}$ , more than



**Fig. 4.** Phase composition and microstructure analysis: (a) XRD pattern; (b) EBSD diffraction calibrated Chiyoda bands of  $Si_{1.5}$ ; (c) KAM map; (d) Phase distribution map; (e) Pole figure; (f) Grain size distribution map.

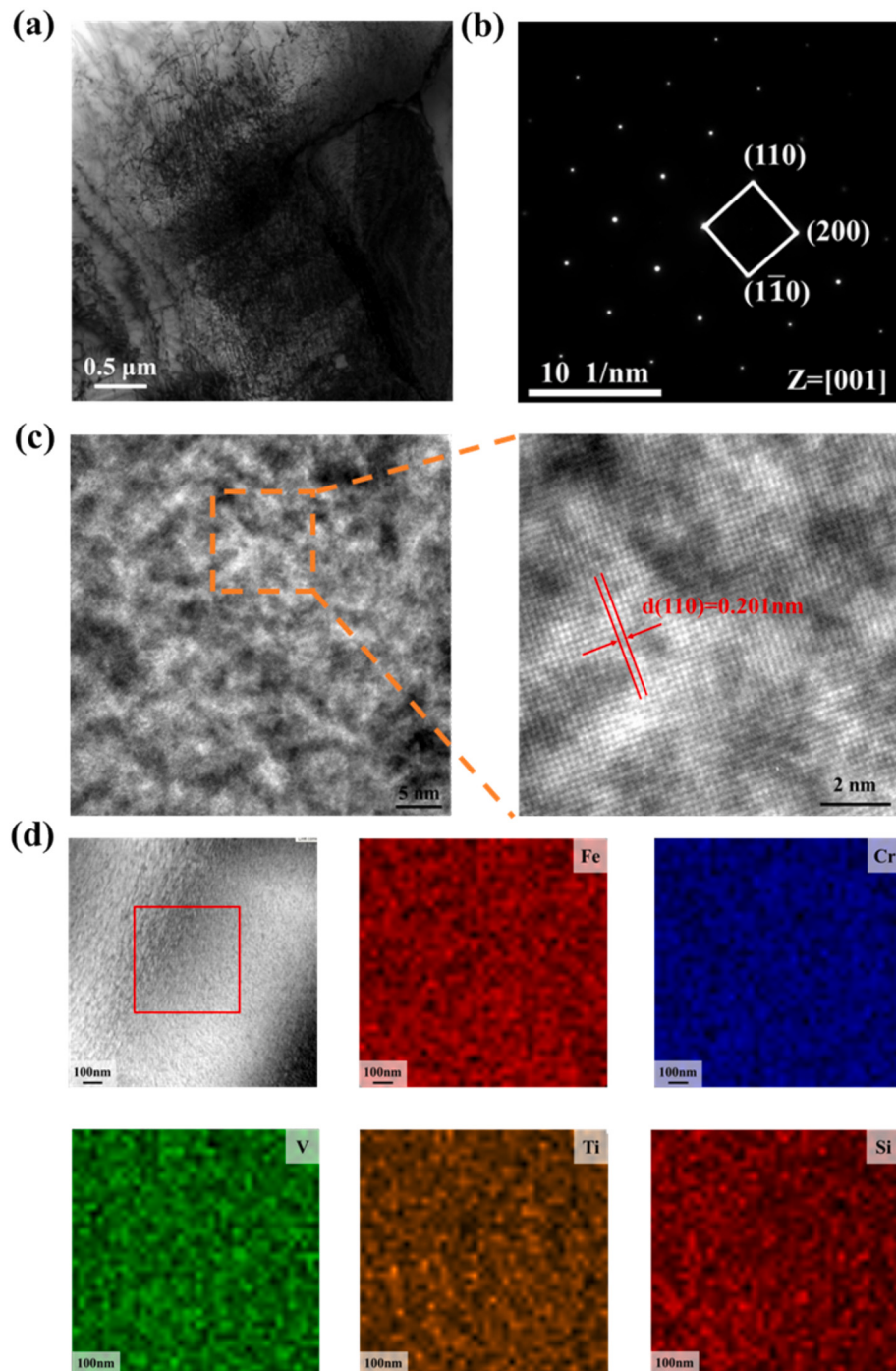


**Fig. 5.** TEM characterization results of  $\text{Si}_{1.5}$ : (a) STEM bright field image; (b) Selected Area Electron Diffraction (SAED) calibration; (c) HRTEM; (d) EDS elemental distribution map.

doubling that of  $\text{Si}_0$ , significantly underscores the coating's enhanced indentation resistance with rising Si content. Microhardness and Young's modulus were determined through nanoindentation tests, as illustrated in Fig. 6(b). The microhardness values increased from 3.80 GPa for  $\text{Si}_0$  to 8.56 GPa for  $\text{Si}_{2.0}$ . The Young's moduli for  $\text{Si}_0$ ,  $\text{Si}_{0.5}$ ,  $\text{Si}_{1.0}$ ,  $\text{Si}_{1.5}$ , and  $\text{Si}_{2.0}$  were 228, 225, 234, 235, and 244 GPa, respectively. When compared with Young's modulus values obtained through density functional theory calculations, the discrepancies were 16.9%, 6.6%, 9.3%, 8.8%, and 11.9%, respectively. These errors are relatively small and the overall trend is in good agreement with the theoretical predictions. When compared with similar or containing-Si HEAs in Table S11, the

nanoindentation results highlight the superior mechanical performance of this alloy system.

Further analysis of the impact of Si element on mechanical properties of alloy systems was conducted using Vickers hardness tests. Vickers microhardness tests, illustrated in Fig. 6(c), reveal hardness values of 2.17, 3.01, 3.58, 4.98, and 7.97 GPa for  $\text{Si}_0$ ,  $\text{Si}_{0.5}$ ,  $\text{Si}_{1.0}$ ,  $\text{Si}_{1.5}$ , and  $\text{Si}_{2.0}$ , respectively. The hardness of  $\text{Si}_{2.0}$  coating, exceeding three times that of  $\text{Si}_0$ , indicates the solid solution of Si in the FeCrVTi system significantly enhances the alloy's hardness. Table S12 also contrasts the Vickers hardness of comparable HEAs with this study's FeCrVTi $\text{Si}_x$  HEAs, showing a superior Vickers hardness for the latter. Fig. 6(d) depicts the

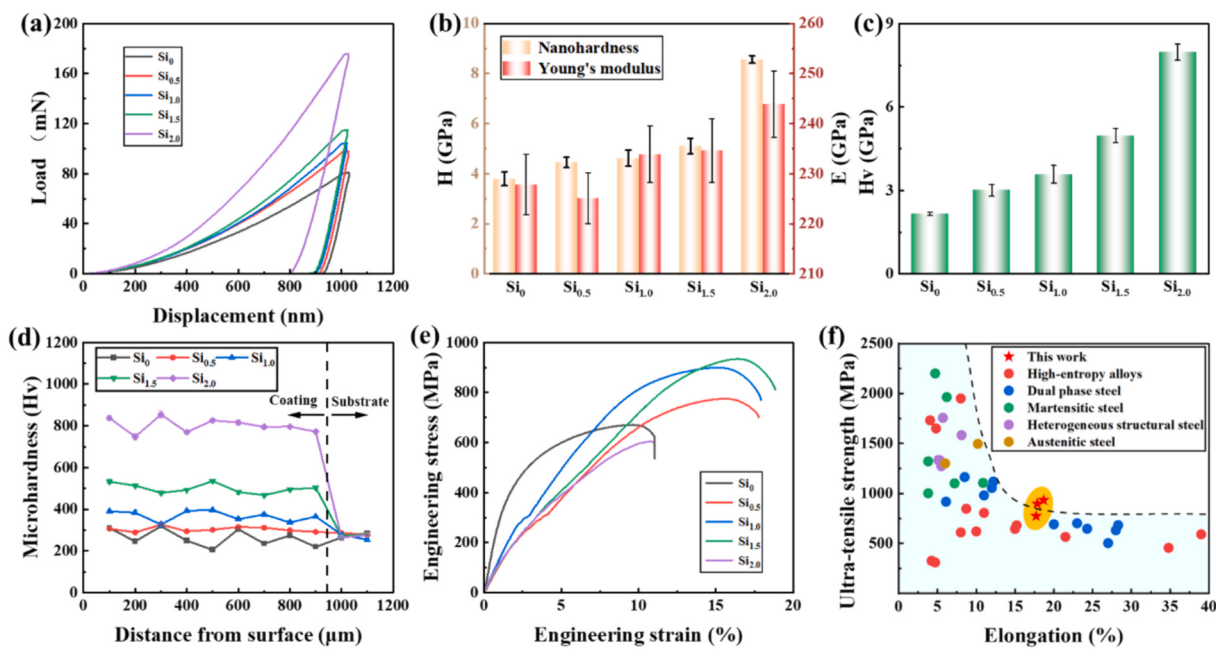


**Fig. 6.** Experimental mechanical properties: (a) load-displacement curves; (b) Young's modulus and nano-hardness; (c) Vickers hardness; (d) hardness distribution of the coating cross-section; (e) tensile stress-strain curves; and (f) The comparison of tensile properties in various system.

hardness distribution across the coating's cross-section, revealing a gradual increase with Si content, culminating in the  $\text{Si}_{2.0}$  coating achieving a peak hardness of 854.3 Hv, about threefold that of the substrate.

Tensile tests were employed to evaluate the strength and ductility of the coating, with the detailed tensile results in Table 1. As shown in Fig. 6(e), the engineering stress-strain curves for this alloy system demonstrate a progressive increase in ultimate tensile strength and elongation with increasing Si content. The optimal strength and ductility were achieved at  $\text{Si}_{1.5}$ , with an ultimate tensile strength of 933 MPa and a tensile elongation of 17.9 %, compared to  $\text{Si}_0$ , which had a 669 MPa ultimate tensile strength and 11.0 % tensile elongation. This effectively enhances the strength of the HEAs system while maintaining good ductility. Fig. S11 depicts the fracture morphologies post-tensile testing, displaying consistent ductile fracture characteristics marked by dimpling, with no significant changes observed. The superior strength-ductility synergy of the  $\text{Si}_{1.5}$  HEA is effectively demonstrated by comparing it with other Si-containing HEAs [66–72], dual-phase steels [73–76], martensitic steels [77–81], heterogeneous structure steels [82], and austenitic steels [83] in similar systems, as shown in Fig. 6(f). It was found that  $\text{Si}_{1.5}$  effectively overcame the “strength-ductility trade-off” dilemma, exhibiting commendable mechanical performance.

#### 3.4. Mechanisms of VEC modulation of mechanical properties

Fig. 7 illustrates the mechanism through which changes in valence electron concentration modulate the chemical microenvironment of the HEAs system, thereby influencing slip behavior and consequently

**Table 1**

The yield strength (YS), ultimate tensile strength (UTS) and elongation of FeCrVTiSi<sub>x</sub> HEAs.

Alloys	YS (MPa)	UTS (MPa)	Elongation (%)
Substrate	276	531	16.5
$\text{Si}_0$	330	669	11.0
$\text{Si}_{0.5}$	238	774	17.7
$\text{Si}_{1.0}$	303	898	17.9
$\text{Si}_{1.5}$	318	933	18.7
$\text{Si}_{2.0}$	210	604	10.8

affecting mechanical properties. For BCC structures, it is well-established that the slip plane is the most densely packed (110) plane. Each plane offers two possible slip directions, and with six equivalent densely packed planes per unit cell, this results in a total of 12 slip directions in BCC structures [61]. The ease of slip significantly affects the mechanical properties of the system. In the absence of Si, DFT calculations reveal that metallic bonds are distributed throughout the system to allow easy slip deformation in two directions on each slip plane, resulting in lower overall strength while maintaining ductility. Upon introducing an appropriate amount of Si, DFT results indicate that it could form stronger covalent bonds with adjacent metal atoms can be formed due to greater electronegativity and half-filled outer electrons than other metal atoms, promoting stronger covalent bonding. More energy is needed to break these stronger covalent bonds during slip, which increases the difficulty of slip and thereby enhances strength. Compared to the pure metal solid solution without Si, a mechanism akin to Orowan strengthening occurs. The challenging bond-breaking process around Si atoms affects the difficulty and progression of subsequent dislocation slips. As dislocations pass around Si atoms, some dislocations may bypass, extending the dislocation line and raising the stress needed to drive dislocation movement, thereby enhancing the strength of the system. Nonetheless, metal atoms adjacent to Si are interconnected with metallic bonds and can still undergo slip, ensuring the alloy's ductility and overcoming the “strength-ductility trade-off” dilemma. Conversely, when an excessive amount of Si is added, DFT calculations reveal significant aggregation of Si atoms, which form strong covalent bonds with each other. The robust covalent bonds with Si atoms make it difficult to break the valence bonds required for slip when dislocations reach regions of Si aggregation, hindering slip and causing an accumulation of dislocations, which reduces the overall ductility of the alloy system. Furthermore, due to the brittleness of Si, the tensile strength of the interconnected Si is relatively low, making it prone to becoming the initiation point of fracture during tension, thereby reducing the system's overall tensile strength. Therefore, by incorporating a suitable proportion of Si and ensuring its even distribution, the system's chemical microenvironment can be effectively altered, regulating slip behavior and ultimately controlling the mechanical properties, thereby overcoming the “strength-ductility trade-off” dilemma.

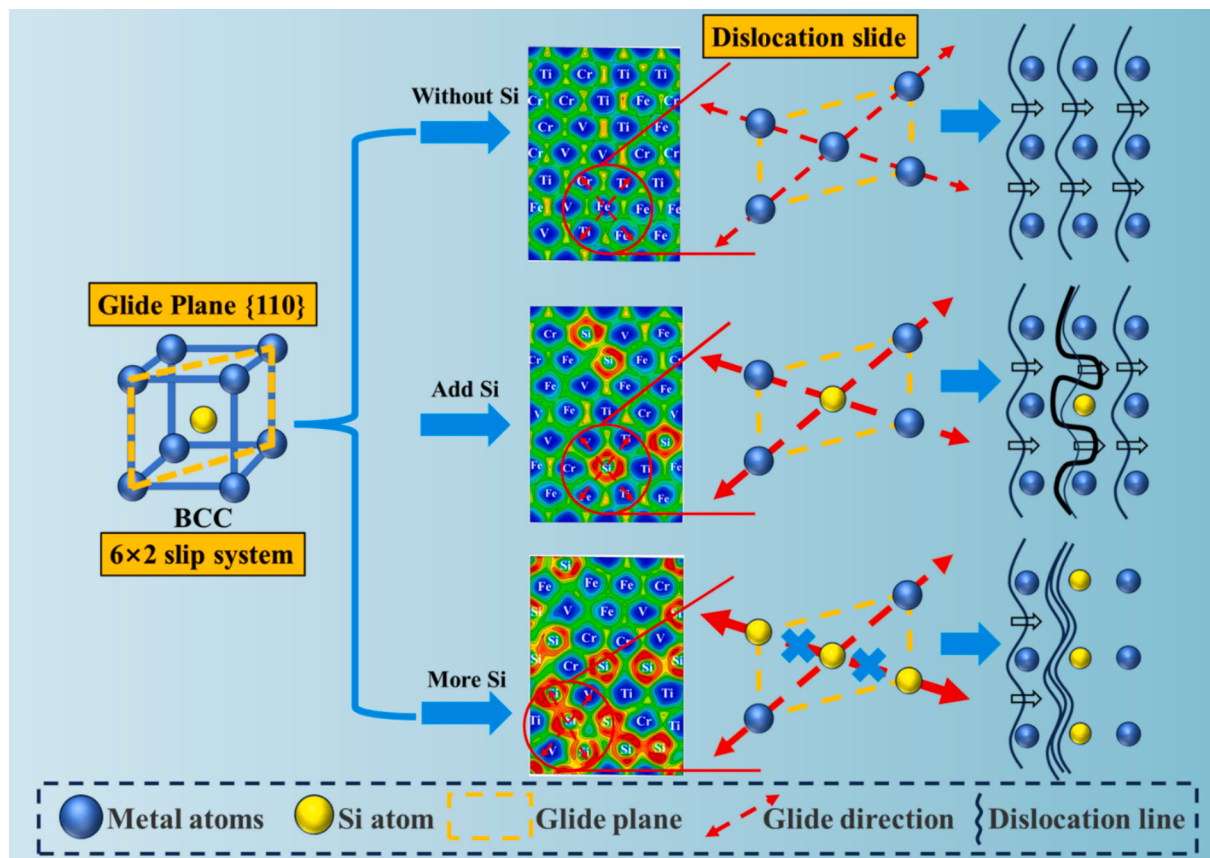


Fig. 7. Mechanism of Si to influencing mechanical properties by modifying the chemical microenvironment to regulate slip behavior.

#### 4. Conclusion

In this study, we propose a strategy based on the regulation of the chemical microenvironment through valence electron concentration to overcome the “strength-ductility trade-off” dilemma in HEAs coating, while simultaneously improving the strength and ductility of metallic materials. The strategy’s efficacy was initially substantiated through density functional theory calculations followed by experimental verification. The main conclusions are as follows:

1. DFT calculations show that the regulation of the chemical microenvironment of HEAs could change the mechanical and ductility properties.
2. The designed FeCrVTiSi<sub>x</sub> alloys consistently exhibit a single BCC solid solution structure, which is characterized by good chemical stability and mechanical stability.
3. The addition of Si enhanced the mechanical properties of the alloy system, effectively overcoming the strength-ductility trade-off. Vickers hardness escalated from 2.16 GPa in Si<sub>0</sub> to 7.97 GPa in Si<sub>2.0</sub>, nano-hardness from 3.80 GPa in Si<sub>0</sub> to 8.56 GPa in Si<sub>2.0</sub>, and Young’s modulus from 228 GPa in Si<sub>0</sub> to 244 GPa in Si<sub>2.0</sub>. Optimal strength-ductility was achieved at a Si<sub>1.5</sub> concentration, exhibiting an ultimate tensile strength of 933 MPa and a tensile elongation of 18.7 %. This represents a 39 % improvement in ultimate tensile strength over Si<sub>0</sub>, alongside enhanced ductility.
4. We analyzed the mechanism by which low VEC in Si mitigates the strength-ductility trade-off. Si modifies the chemical microenvironment, influencing slip transmission and thereby exerting control over mechanical properties. The introduction of an optimal quantity of dispersed Si into the alloy system increases the difficulty of slip transmission but still ensures its normal progression, thereby overcoming the “strength-ductility trade-off” dilemma.

#### CRediT authorship contribution statement

**Shouyuan Lin:** Writing – original draft, Software, Methodology, Investigation, Conceptualization. **Yuan Yao:** Writing – review & editing, Visualization, Validation, Supervision, Formal analysis, Data curation. **Zhongping Yao:** Writing – review & editing, Visualization, Validation, Supervision, Formal analysis, Data curation. **Guanghui Shi:** Software, Investigation. **Yanyan Liu:** Software, Investigation. **Peng Zhang:** Software, Investigation. **Songtao Lu:** Supervision, Resources, Data curation. **Wei Qin:** Supervision, Resources, Data curation. **Xiaohong Wu:** Supervision, Resources, Data curation.

#### Declaration of competing interest

The authors declare that they have no known competing financial interests or personal relationships that could have appeared to influence the work reported in this paper.

#### Data availability

Research data are not shared.

#### Acknowledgements

This work was financially supported by the National Natural Science Foundation of China (Grant Nos. U2067216 and U2130109) and the National Key Research and Development Program of China (No. 2022YFB3806300). The authors also acknowledge Beijing PARATERA Tech Co., Ltd. for providing HPC resources that have contributed to the research results reported within this paper. URL: <https://www.paratera.com/>.



